

# SCREP: Scene Coordinate Regression and Evidential Learning-based Perception-Aware Trajectory Generation

Juyeop Han<sup>1</sup>, Lukas Lao Beyer<sup>1</sup>, Guilherme V. Cavaleiro<sup>1</sup>, and Sertac Karaman<sup>1</sup>

**Abstract**— Autonomous flight in GPS-denied indoor spaces requires trajectories that keep visual-localization error tightly bounded across varied missions. Whereas visual inertial odometry (VIO) accumulates drift over time, scene coordinate regression (SCR) yields drift-free, high-accuracy absolute pose estimation. We present a perception-aware framework that couples an evidential learning-based SCR pose estimator with a receding horizon trajectory optimizer. The optimizer steers the onboard camera toward pixels whose uncertainty predicts reliable scene coordinates, while a fixed-lag smoother fuses the low-rate SCR stream with high-rate IMU data to close the perception-control loop in real time. In simulation, our planner reduces translation (rotation) mean error by 54% / 15% (40% / 31%) relative to yaw-fixed and forward-looking baselines, respectively. Moreover, hardware-in-the-loop experiment validates the feasibility of our proposed framework.

## I. INTRODUCTION

Vision-based localization has made rapid progress in recent years, allowing unmanned aerial vehicles (UAVs) to fly autonomously in GPS-denied indoor environments. Most perception-aware trajectory planning approaches, [1], [2], [3], steer the camera toward feature-rich regions to improve the pose estimate obtained by visual inertial odometry (VIO). Although effective at reducing drift over short distances, these methods are still limited by the cumulative error of VIO.

An alternative is to employ scene coordinate regression (SCR), a learning-based method predicting a 3D coordinate for every pixel [4], [5], [6], [7], [8] instead of VIO. A Perspective-n-Point (PnP) solver then produces a drift-free absolute camera pose, achieving high metric accuracy even over long trajectories. However, not all pixels produce reliable coordinates. Moreover, SCR poses have both outliers and a low frequency latency, which complicates their use with real-time planning and control.

This paper proposes a perception-aware trajectory planning framework that explicitly utilizes the pixel-wise uncertainty of an evidential learning-based SCR network (E-SCRNet). To the best of our knowledge, this is the first active-perception research using SCR. We train a

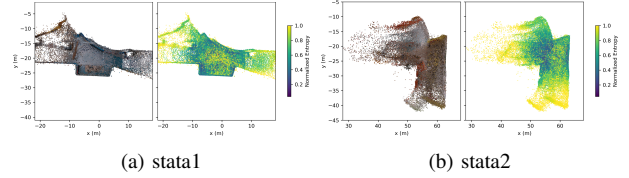


Fig. 1: Top-down 3-D reconstructions of the two sites produced by SCR. (left) RGB-colored points (right) normalized entropy map.

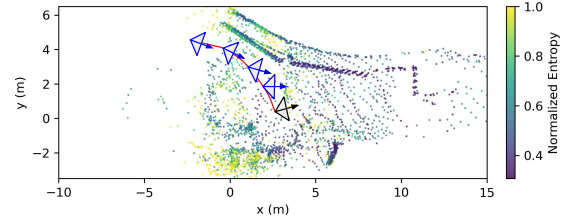


Fig. 2: Illustration of proposed receding horizon perception-aware trajectory generation. (blue) Camera orientations are optimized to steer the camera toward low entropy coordinates. (red) position trajectory (black) current pose.

neural network for SCR with evidential learning [9], so each pixel outputs scene coordinates and both aleatoric and epistemic uncertainties. We use the entropy as the uncertainty metric since it jointly captures aleatoric and epistemic uncertainties. The entropy map drives a receding horizon trajectory optimizer that (i) weights low-entropy pixels higher and (ii) removes high-entropy pixels from the cost, thereby orienting the camera toward informative viewpoints while following the given reference position trajectory. A fixed-lag smoother then fuses the low-rate SCR pose with high-rate IMU measurements, reducing latency, suppressing outlier SCR pose estimates and eliminating the drift caused by IMU bias.

The main contributions of this research are as follows:

- We present a real-time and receding-horizon framework that injects E-SCRNet uncertainty into perception-aware trajectory optimization, sustaining high-accuracy localization.
- We empirically show that entropy is a more informative uncertainty metric than separate aleatoric and epistemic uncertainty measures.
- We validate our approach through simulation and hardware-in-the-loop experiments, where the proposed planner outperforms baselines in localization.

<sup>1</sup>The authors are with Laboratory for Information and Decision Systems (LIDS), Massachusetts Institute of Technology, Cambridge, MA 02139, USA {juyeop, llb, guivenca, sertac}@mit.edu

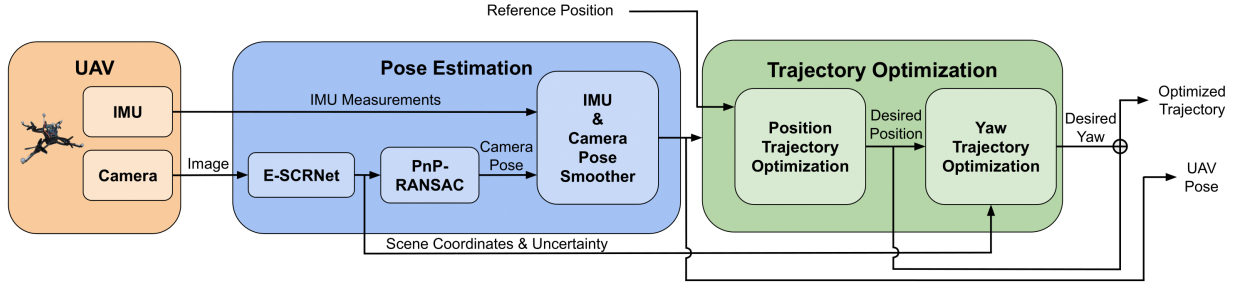


Fig. 3: System architecture. (1) a pose estimation block consisting of E-SCRNet, PnP-RANSAC, and a fixed-lag smoother; (2) a two-stage trajectory optimization block for position and yaw.

## II. RELATED WORK

### A. Perception-Aware Trajectory Planning

PAMPC [1] augments nonlinear model predictive control (MPC) with a visibility cost and Zhang et al. [2] frame perception-aware planning in a receding-horizon fashion. Yaw optimization was later coupled with differential flatness and a differentiable camera cost [3], extended to incorporate semantic priors [10], time-optimal parameterization [11]. Other directions include Fisher information [12], topological path planning [13]. Recent studies combine position-yaw optimization with a novel feature-visibility model [14], feature-limited or unknown environments [15] and introduces control barrier functions for safety guarantees [16]. However, all of the above rely on visual-inertial odometry (VIO), and the accumulated drift of VIO is merely reduced rather than eliminated.

### B. Learning-based Visual Localization

Beyond such model-based visual localization methods, numerous learning-based visual localization methods have emerged. Absolute Pose Regressors (APRs) employ neural networks to directly regress camera pose [17], [18], [19]. Uncertainty-aware variants [20], [21] also estimate uncertainty, yet APRs remain markedly less accurate than both model-based pipelines and other learning-based alternatives [22].

HLoc [23] retrieves candidate keyframes with global descriptors and refines the pose via local feature matching. While accurate, its memory and computation grow with the number of keyframes, being likely to exceed the resources available on onboard hardware as the environment expands.

SCR regresses a dense 3-D scene-coordinate map and then estimates the pose with PnP-RANSAC. Early work used random forests [4]. DSAC replaced it with differentiable RANSAC and CNNs [5], [6]. Hierarchical SCR has recently been explored for large scenes [7], [8]. SCR attains high absolute accuracy with a single forward pass but can produce outliers.

### C. Uncertainty Quantification

Bayesian neural networks (BNNs) estimate aleatoric and epistemic uncertainty via Monte-Carlo dropout [24], deep ensembles [25], or more general Bayesian learning frameworks [26]. Uncertainty-aware APR [20] and VIO using BNNs and neural radiance field [27] show the benefit of uncertainty for localization. However, BNNs require multiple forward passes for the uncertainty quantification.

On the other hand, evidential learning offers closed-form aleatoric and epistemic estimates without sampling [9], [28] and has been adopted for NeRF-aided SCR [29], semantic segmentation [30], semantic mapping [31], and traversability learning [32].

## III. SYSTEM OVERVIEW

Given generic navigation scenarios, this study aims to improve an initial positional path by simultaneously refining the vehicle's position and yaw trajectories.

**Problem.** Within each receding horizon of length  $T_{plan}$ , the UAV is given (i) reference position waypoints or trajectory, (ii) regressed scene-coordinates and their pixel-wise uncertainties, and (iii) the current UAV pose estimate. The objective is to produce a dynamically feasible trajectory that (a) follows the reference, (b) respects velocity/acceleration limits, and (c) orients viewpoints with low uncertainty to maximize localization accuracy. We assume (A1) lower uncertainty implies higher scene-coordinate accuracy and (A2) uncertainty varies smoothly, allowing its use within short horizons. Thanks to the differential flatness of multirotor dynamics [33], the position and yaw trajectories  $\{\mathbf{p}(t), \psi(t)\}$ , and their derivatives fully determine the required state and control.

**Pipeline.** Fig. 3 depicts the pipeline for the receding horizon trajectory generation achieving the objective. Images from a camera pass through E-SCRNet [29] to produce scene coordinates and uncertainties, which a PnP-RANSAC module converts into camera poses. To compensate for the latency and outliers of this stream, we fuse it with high-rate IMU measurements

in a fixed-lag GTSAM smoother [34], yielding a clean, high-frequency state estimate. Note that other sensor fusion methods, such as the Kalman Filter, would also suffice for the UAV pose estimation.

The pose estimate, waypoints, scene coordinates, and uncertainties feed a perception-aware optimizer, split into position and yaw sub-problems for real-time execution. The resulting reference trajectories  $\{\mathbf{p}^*(t), \psi^*(t)\}$  is repeatedly generated until the UAV reaches its goal pose.

#### IV. METHODOLOGY

In this section, we first describe the training of E-SCRNet, a SCR network trained via deep evidential regression [9], and discuss its representation of uncertainty for the perception-aware trajectory planning. We then present our B-spline-based, receding horizon, perception-aware trajectory planner utilizing these scene coordinates and their associated uncertainties.

##### A. Scene Coordinate Regression with Deep Evidential Regression

In this study, we train a neural network for SCR and assess the uncertainty of each predicted scene coordinate so that the perception-aware trajectory optimization can reason about perception quality. We adopt the deep evidential regression [9], following the approach in [29], as it can jointly quantify both aleatoric and epistemic uncertainties without requiring multiple forward passes, unlike BNNs. Note that the architecture of the SCR network is tangential to this work.

Let  $\mathbf{v} \in \mathbb{R}^3$  denote the scene coordinate of each pixel. For brevity, we write  $v$  when referring to one Cartesian component. We model  $v \sim \mathcal{N}(\mu, \sigma^2)$  where the unknown mean and variance,  $\mathbf{t} = (\mu, \sigma^2)$ , are themselves random variables drawn from a Gaussian and inverse gamma prior,  $\mu \sim \mathcal{N}(\gamma, \sigma^2/\lambda)$ ,  $\sigma^2 \sim \Gamma^{-1}(\alpha, \beta)$ . Here,  $\Gamma(\cdot)$  is the gamma function. Assuming that the priors on  $\mu$  and  $\sigma^2$  factorize each other,  $p(\mathbf{t}|\mathbf{m})$  is the Normal Inverse-Gamma (NIG) distribution, which is a Gaussian conjugate prior, parameterized by  $\mathbf{m} = (\gamma, \lambda, \alpha, \beta)$  with  $\lambda > 0$ ,  $\alpha > 1$ , and  $\beta > 0$ .

This NIG distribution serves as a higher-order evidential distribution from which the lower-order Gaussian likelihood that generates scene coordinates is sampled, allowing the network to express the prediction  $\mathbb{E}[\mu] = \gamma$ , the aleatoric uncertainty  $\mathbb{E}[\sigma^2] = \beta/(\alpha - 1)$ , and epistemic uncertainty  $\text{Var}[\mu] = \beta/(\lambda(\alpha - 1))$ .

The deep evidential regression aims to learn the hyperparameters  $\mathbf{m}_\theta = (\gamma_\theta, \lambda_\theta, \alpha_\theta, \beta_\theta)$ . We can express the likelihood of the scene coordinate given the hyperparameters  $\mathbf{m}_\theta$  as a closed-form  $p(v|\mathbf{m}_\theta) = \text{St}(v; \gamma_\theta, \beta_\theta(1 + \lambda_\theta)/(\lambda_\theta \alpha_\theta), 2\alpha_\theta)$  where  $\text{St}(v; \eta, \tau^2, \chi)$  is a Student-t distribution with location  $\eta$ , scale  $\tau^2$ , and degree of freedom  $\chi$ .

The total loss is the mean of the per-sample loss,  $\mathcal{L}_\theta = \frac{1}{N} \sum_{i=1}^N \mathcal{L}_\theta^i$ , where each sample-wise loss is  $\mathcal{L}_\theta^i = \mathcal{L}_{\theta, \text{nll}}^i + \rho \mathcal{L}_{\theta, \text{reg}}^i$ . The loss  $\mathcal{L}_{\theta, \text{nll}}^i$  is chosen as the negative log-likelihood (NLL) of  $p(v|\mathbf{m}_\theta)$  for maximum likelihood estimation (MLE):

$$\begin{aligned} \mathcal{L}_{\theta, \text{nll}}^i &= \log(\Gamma(\alpha_\theta)/\Gamma(\alpha_\theta + \frac{1}{2})) \\ &\quad + \frac{1}{2} \log(\pi/\lambda_\theta) - \alpha_\theta \log(2\beta_\theta(1 + \lambda_\theta)) \\ &\quad + (\alpha_\theta + \frac{1}{2}) \log((v_i - \gamma_\theta)^2 + 2\beta_\theta(1 + \lambda_\theta)). \end{aligned} \quad (1)$$

The loss  $\mathcal{L}_{\theta, \text{reg}}$  is designed for regularization:

$$\mathcal{L}_{\theta, \text{reg}}^i = (2\lambda_\theta + \alpha_\theta)|v_i - \gamma_\theta|. \quad (2)$$

After training, we can express the predictive entropy,  $H_\theta = \mathbb{E}_{v \sim p(v|\mathbf{m}_\theta)}[-\log p(v|\mathbf{m}_\theta)]$ , admits the closed form

$$\begin{aligned} H_\theta &= (\alpha_\theta + \frac{1}{2})(\psi(\alpha_\theta + \frac{1}{2}) - \psi(\alpha_\theta)) \\ &\quad + \frac{1}{2} \log(2\pi\beta_\theta(1 + \lambda_\theta)/\lambda_\theta) \\ &\quad + \log(\Gamma(\alpha_\theta)/\Gamma(\alpha_\theta + \frac{1}{2})) \end{aligned} \quad (3)$$

where  $\psi(\cdot)$  is the digamma function. We use the entropy as a representation of uncertainty instead of aleatoric and epistemic uncertainty since it can represent the aleatoric and epistemic uncertainty. The detailed justification will be given in Section V-B. We refer the reader to [9] for more information on deep evidential regression.

##### B. Trajectory Optimization

After receiving the current UAV pose from a fixed-lag smoother, reference waypoints, scene coordinates and their uncertainty, position and yaw trajectories are optimized to track waypoints and orient reliable scene coordinates. In this subsection, we detail the perception-aware trajectory optimization.

**Uniform B-Spline.** Both position and yaw are parameterized as clamped, uniform B-splines of degree  $k = 3$ :

$$\mathbf{q}(t) = \sum_{i=0}^n \mathbf{q}_i N_{i,k}(t) \quad (4)$$

where the knot vector is  $\{t_0, t_1, \dots, t_{n+k+1}\}$ , the control points are  $\mathbf{q}_i = \{q_{x,i}, q_{y,i}, q_{z,i}, q_{\psi,i}\} \in \mathbb{R}^4$ , and  $N_{i,k}(t)$  denotes the B-spline basis functions. Each knot span has equal duration  $\Delta t = t_{i+1} - t_i$ . For clamping, the first and last  $k$  knots are repeated:  $t_0 = \dots = t_{k-1}$  and  $t_{n+1} = \dots = t_{n+k+1}$ . We fix the first control point to the current UAV pose and the last control point to the final waypoint within the planning horizon  $T_{\text{plan}}$ . Then, the other control points become optimization variables to minimize the cost function.

**Optimization Cost.** Similar to Bartolomei et al. [10], the total cost function,  $C_{\text{total}}$ , is represented as the weighted sum of the cost functions for different purposes. To reduce computational load, we optimize the

position and yaw separately by minimizing two disjoint sub-objectives rather than the full  $C_{total}$ :

$$\begin{aligned} C_{total}^{\mathbf{p}} &= \lambda_{wp} C_{wp}^{\mathbf{p}} + \lambda_{eq} C_{eq}^{\mathbf{p}} + \lambda_{ie} C_{ie}^{\mathbf{p}} + \lambda_s C_s^{\mathbf{p}} \\ C_{total}^{\psi} &= \lambda_{fov} C_{fov}^{\psi} + \lambda_{eq} C_{eq}^{\psi} + \lambda_{ie} C_{ie}^{\psi} + \lambda_s C_s^{\psi}. \end{aligned} \quad (5)$$

where the superscripts,  $\mathbf{p}$  and  $\psi$ , indicate that the terms are evaluated on the position and yaw trajectory, respectively. We are going to drop the superscript for brevity. The coefficients  $\lambda_{(\cdot)}$  balance five components:  $C_{wp}$  penalizes deviation from the given waypoints,  $C_{fov}$  rewards keeping reliable scene coordinates within the camera's field-of-view (FOV),  $C_{eq}$  enforces the trajectory starts from the given initial velocity, acceleration, and jerk,  $C_{ie}$  enforces the specified velocity and acceleration bounds, and  $C_s$  promotes smoothness of the trajectory.

Let  $\{\mathbf{w}_0, \dots, \mathbf{w}_{r-1}\}$  denote all waypoints and let  $\{s_1, \dots, s_{r-2}\}$  be their prescribed arrival times except the first and last. The waypoint cost  $C_{wp}$  penalizes the squared Euclidean error between the position trajectory and each desired waypoint:

$$C_{wp} = \sum_{i=1}^{r-2} \sum_{o \in \{x, y, z\}} (q_o(s_i) - w_{o,i})^2. \quad (6)$$

Our formulation of the FOV cost  $C_{fov}$  is inspired by Murali et al. [3]. Whereas the original cost encourages the camera to track as many covisible features as possible within its frustum, our version instead rewards keeping low-uncertainty scene coordinates in view regardless of covisibility.

We assume the camera is mounted on the UAV with a known relative pose. Given the trajectories, we can compute the camera position  $\mathbf{p}_{C,i} \in \mathbb{R}^3$  and orientation  $R_i^C \in \text{SO}(3)$  with respect to the world frame at each time  $t = s_i$ . Let  $\mathbf{v}_j \in \mathbb{R}^3$  be the  $j$ -th scene-coordinate point in the world frame; the same point expressed in the camera frame is then  $\mathbf{v}_{i,j}^C = R_i^C (\mathbf{v}_j - \mathbf{p}_{C,i})$ .

Next, we need to build a differentiable indicator function of whether scene coordinates  $\mathbf{v}_{i,j}^C$  are within the camera frustum for the numerical optimization. For this purpose, the displacement vectors from the optical center to the four image-plane corners:

$$\begin{aligned} \mathbf{z}_{TR} &= [(w - c_x)l_x \quad (-c_y)l_y \quad f]^T \\ \mathbf{z}_{LR} &= [(w - c_x)l_x \quad (h - c_y)l_y \quad f]^T \\ \mathbf{z}_{TL} &= [(-c_x)l_x \quad (-c_y)l_y \quad f]^T \\ \mathbf{z}_{LL} &= [(-c_x)l_x \quad (h - c_y)l_y \quad f]^T \end{aligned} \quad (7)$$

where  $w$  and  $h$  are the image width and height in pixels,  $(c_x, c_y)$  is the principal point in pixels,  $l_x$  and  $l_y$  are the physical pixel sizes (m/pix), and  $f$  is the focal length in meters. The normal vectors of the four side half planes of the camera frustum are  $\mathbf{z}_{TR} \times \mathbf{z}_{LR}$ ,  $\mathbf{z}_{TL} \times \mathbf{z}_{TR}$ ,  $\mathbf{z}_{LL} \times \mathbf{z}_{TL}$ ,

and  $\mathbf{z}_{LR} \times \mathbf{z}_{LL}$ . Using these normals, we construct a soft, indicator vector

$$\mathbf{o}_{i,j} = \begin{bmatrix} \frac{1}{2}[1 + \tanh((\mathbf{z}_{TR} \times \mathbf{z}_{LR}) \cdot \mathbf{v}_{i,j}^C / s)] \\ \frac{1}{2}[1 + \tanh((\mathbf{z}_{TL} \times \mathbf{z}_{TR}) \cdot \mathbf{v}_{i,j}^C / s)] \\ \frac{1}{2}[1 + \tanh((\mathbf{z}_{LL} \times \mathbf{z}_{TL}) \cdot \mathbf{v}_{i,j}^C / s)] \\ \frac{1}{2}[1 + \tanh((\mathbf{z}_{LR} \times \mathbf{z}_{LL}) \cdot \mathbf{v}_{i,j}^C / s)] \\ \frac{1}{2}[1 + \tanh((\mathbf{v}_{i,j}^C - f\mathbf{e}_3) \cdot \mathbf{e}_3 / s)] \end{bmatrix}, \quad (8)$$

where  $\mathbf{e}_3 = [0, 0, 1]^T$  and  $s > 0$  are the camera's forward axis and a smoothing constant, respectively. For the  $j$ -th scene coordinate at time  $t = s_i$ , the desired scalar indicator is defined as the product of each element of  $\mathbf{o}_{i,j}$  as

$$F(\mathbf{c}_i, \mathbf{v}_j) = \prod_{k=1}^5 o_{i,j,k}. \quad (9)$$

The scalar indicator approaches 1 when the point lies inside the frustum and 0 otherwise. A larger  $s$  yields a smoother transition but a less selective indicator.

The cost is the weighted sum of the indicators over all sampling times and scene coordinates:

$$C_{fov} = - \sum_{i=1}^{r-1} \sum_{j=1}^{n_f} \exp(-aH_{\theta,j}) F(\mathbf{c}_i, \mathbf{v}_j). \quad (10)$$

Here,  $n_f$  denotes the number of selected scene coordinates. These coordinates are randomly chosen among those with entropy values below a predefined threshold. The weight  $\exp(-aH_{\theta,j})$  depends on the entropy  $H_{\theta,j}$  on Eq. (3);  $a > 0$  is constant. Lower entropy, i.e., higher certainty, yields a larger weight, encouraging the yaw trajectory to keep such scene coordinates in view.

Because we solve the optimization repeatedly over a moving horizon  $T_{\text{exec}}$ , each new trajectory must splice smoothly onto the previous one. To enforce continuity, the initial-equality cost  $C_{eq}$  penalizes any mismatch between the prescribed initial derivatives and those of the candidate trajectory at  $t = t_0$ :

$$C_{eq} = \|\mathbf{v}(t_0) - \mathbf{v}_0\|_2^2 + \|\mathbf{a}(t_0) - \mathbf{a}_0\|_2^2 + \|\mathbf{j}(t_0) - \mathbf{j}_0\|_2^2 \quad (11)$$

where  $\mathbf{v}_0, \mathbf{a}_0, \mathbf{j}_0 \in \mathbb{R}^4$  denote the desired initial velocity, acceleration, and jerk for the translation coordinates and yaw. Note that the initial position and yaw automatically match their desired values because a clamped B-spline is anchored to the first control point.

The inequality cost  $C_{ie}$  enforces that every component of the planned trajectory respects user-specified velocity and acceleration limits:

$$C_{ie} = \sum_{i=1}^{r-1} \sum_{o \in \{x, y, z, \psi\}} (M_v(v_o(s_i)) + M_a(a_o(s_i))), \quad (12)$$

where  $v_o(s_i)$  and  $a_o(s_i)$  denote, respectively, the velocity and acceleration of coordinate  $o$  at sample time  $s_i$ .

The single auxiliary function,  $M_x(x) = \text{ReLU}((x^2 - x_{\max}^2)^2)$ , is applied to both velocity and acceleration.

The smoothness cost  $C_s$  promotes a smooth trajectory by enforcing consistency between consecutive elastic bands,  $\mathbf{S}_{i+1,i}$  and  $\mathbf{S}_{i-1,i}$  with  $\mathbf{S}_{i,j} = \mathbf{q}_i - \mathbf{q}_j$ :

$$C_s = \sum_{i=1}^{n-1} \|\mathbf{S}_{i+1,i} + \mathbf{S}_{i-1,i}\|_2^2. \quad (13)$$

## V. EXPERIMENTS

We evaluated our approach under simulation with two goals: (a) to verify that the entropy defined in Eq. (3) provides an appropriate measure of uncertainty, and (b) to demonstrate the effectiveness of our perception-aware trajectory planner. First, we empirically examined how the proposed entropy compares with conventional aleatoric and epistemic uncertainty measures. We then benchmarked our planner against baselines and performed an ablation study to isolate the impact of the uncertainty within SCR and the optimization. We also conducted the hardware-in-the-loop experiments to confirm the practical feasibility of our methods.

### A. Setup

We ran photorealistic simulations using the Flight-Goggles simulator [36] under Intel Core i9-7920X CPU. The simulated camera resolution was fixed at  $480 \times 480$  pixels, and its FoV was  $90^\circ$ . We trained a E-SCRNet following the architecture in [6] for each of the two sites (“stata1” and “stata2”) in the *stata\_ground\_floor* environment as shown in Fig. 1.

To highlight the advantages brought by our perception-aware planner, we deliberately used a small training set: about 1,200 images captured along a single trajectory (“picasso”) from the Blackbirds dataset [37], trained for only 100k iterations. The regularization coefficient  $\rho$ , the learning rates, and the batch size were  $10^{-2}$ ,  $10^{-4}$ , and 1, respectively. Adam optimizer was applied. The training time was 14 minutes using one NVIDIA RTX 6000 Ada GPU.

For every planning step, we minimize the costs in Eq. (5) with the L-BFGS algorithm provided by NLOpt [38]. The required parameters for the optimization are set in Table II. The number of control points for the clamped B-spline in Eq. (4) was set to six. Scene-coordinate regression is run every 0.2 s.

### B. Uncertainty Representation

We collected scene coordinate predictions and their uncertainty maps from E-SCRNet while the UAV followed a circular trajectory. Fig. 4 analyzes the relationship between the L2 prediction error and three uncertainty estimates: aleatoric, epistemic, and entropy.

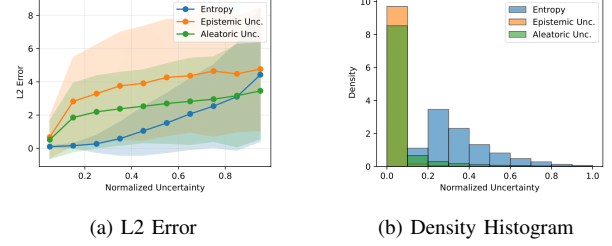


Fig. 4: Graphs for normalized uncertainty and scene coordinate errors of E-SCRNet. (a) Mean and standard deviation of L2 error (b) Density histogram

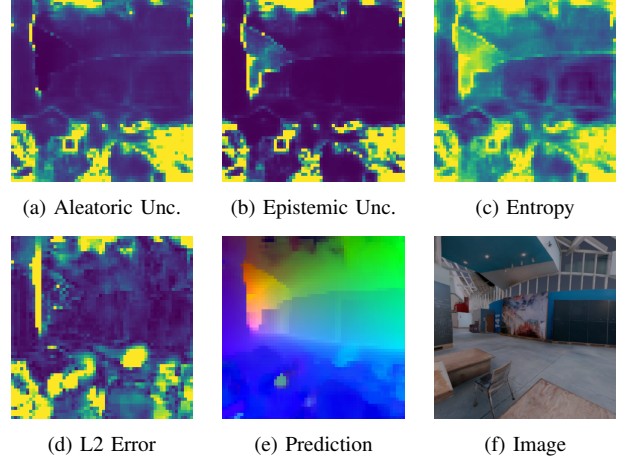


Fig. 5: Qualitative results of E-SCRNet for a test image. (a) Aleatoric Uncertainty (b) Epistemic Uncertainty (c) Entropy (d) L2 Error of predicted scene coordinates (e) Predicted scene coordinates (f) Input image.

We clipped the largest 3% of uncertainty values and normalized the remainder to  $[0, 1]$  for visual clarity.

As shown in Fig. 4a, the mean error increases almost linearly with binned entropy, whereas its correlation with the others is weaker. Moreover, the error’s standard deviation declines as entropy decreases, while it remains high across the full range of the other measures. Fig. 4b further reveals that entropy is less skewed toward zero than the other uncertainties, indicating that it provides a more informative and well-spread metric.

Based on these observations, we adopt entropy as our uncertainty metric for the scene coordinate predictions since entropy simultaneously captures both aleatoric and epistemic effects and closely tracks the error.

### C. Simulation Results.

**Comparison to baselines.** To the best of our knowledge, no prior work has explored perception-aware trajectory generation using SCR. Therefore, we compare our planner with two intuitive yaw strategies: *Constant*, which fixes the camera to a global heading, and *Forward*, which keeps the camera aligned with the velocity vector. We evaluate four trajectories from the Blackbird dataset per site, “clover,” “patrick,” “thrice,” and “winter” in



TABLE I: Localization accuracy for each trajectory (translation / rotation in  $\text{cm}^\circ$ ). Columns group the three yaw strategies, *Constant*, *Forward*, and our perception-aware planner (*Ours*), and distinguish when the accuracy is evaluated solely by SCR or the fixed-lag smoother. Failed cases are not recorded and therefore are not included in the average calculation.

	Constant				Forward				Ours			
	IMU + SCR		SCR		IMU + SCR		SCR		IMU + SCR		SCR	
	RMSE↓	Mean↓	Median↓	Mean↓	RMSE↓	Mean↓	Median↓	Mean↓	RMSE↓	Mean↓	Median↓	Mean↓
clover	31.0/9.2	24.2/7.8	10.7/1.2	17.7/3.2	18.7/4.0	16.5/3.6	8.0/0.6	9.7/0.9	16.1/4.3	14.8/3.7	7.2/0.5	7.5/0.5
patrick	-	-	-	-	18.0/10.5	15.9/8.7	8.8/0.7	10.6/0.8	16.9/1.2	15.5/1.1	7.7/0.5	8.9/0.6
thrice	-	-	-	-	18.7/4.7	17.4/3.8	8.2/0.6	8.8/0.7	18.2/3.3	15.9/2.9	8.0/0.5	8.6/0.5
winter	27.9/2.8	21.1/2.4	9.0/0.9	15.2/2.3	21.4/3.0	19.6/2.7	8.4/0.7	9.7/0.9	18.8/1.4	16.6/1.3	8.3/0.5	9.1/0.6
ampersand	27.9/3.6	24.7/2.9	13.5/1.3	18.3/1.5	20.6/1.7	19.1/1.6	12.8/1.7	13.8/1.8	18.0/1.0	16.6/0.9	11.3/1.6	11.7/1.8
dice	39.1/1.7	33.8/1.5	16.9/1.8	24.0/1.9	39.7/2.3	26.9/2.0	13.0/2.2	22.3/2.9	24.3/3.8	21.7/3.5	13.9/1.7	17.8/1.9
halfmoon	21.5/1.4	19.6/1.3	13.4/1.7	14.4/1.7	23.7/2.8	20.4/2.3	11.4/2.1	15.9/2.2	18.0/4.8	17.1/4.4	12.4/1.9	13.6/1.9
sid	130.8/8.4	84.6/6.1	31.4/2.6	69.2/6.6	41.8/1.8	33.9/1.6	21.9/2.8	30.2/3.6	40.5/1.5	35.9/1.4	26.3/1.7	30.1/1.8
Average	46.4/4.5	34.7/3.7	12.9/1.5	26.5/2.9	25.3/3.9	21.2/3.3	10.1/1.2	15.1/1.7	21.5/2.7	19.2/2.4	9.8/1.1	13.4/1.2

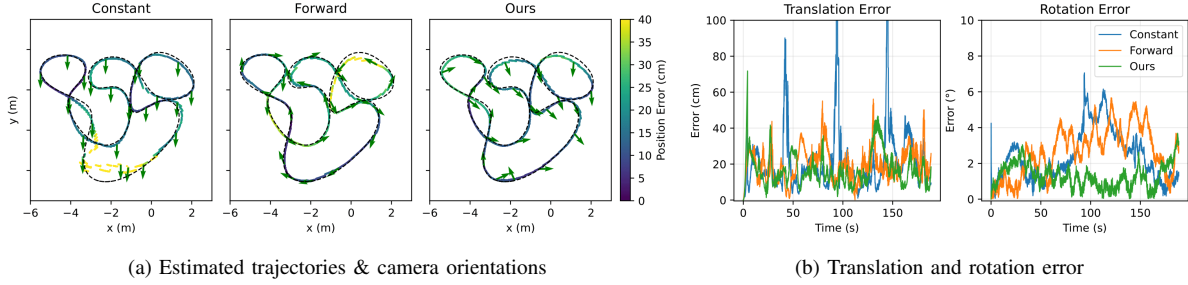


Fig. 6: Comparison of the baseline planners (Constant, Forward) with the proposed method. (a) Top-down view of the reference trajectory (black dotted), the executed trajectories (colored), camera orientation (green arrows). (b) Time histories of translation error (left) and rotation error (right) for Constant (blue), Forward (orange), and Ours (green).

TABLE II: Parameters for trajectory optimization.

$\lambda_{wp}$	$\lambda_{fov}$	$\lambda_{eq}$	$\lambda_{ie}$	$\lambda_s$	$T_{plan}$	$T_{exec}$	$n_f$	$s$	$a$
$10^4$	$10^1$	$10^3$	1.0	5.0	0.8s	0.5s	200	5.0	0.5

*stata1*, and “ampersand,” “dice,” “halfmoon,” and “sid” in *stata2*. Each trajectory is flown multiple times.

Table I reports localization accuracy for both the raw SCR output through PnP-RANSAC (“SCR”) and the fixed-lag smoother that fuses IMU and SCR (“IMU + SCR”). A run is deemed failed when the smoother diverges. Our perception-aware planner and *Forward* showed 100% of success rate, whereas the *Constant* showed 75% of success rate. Even on successful runs, our method consistently achieved lower translation and rotation errors. Our method lowers translation RMSE by 54% relative to the *Constant* and 15% relative to *Forward*; rotation RMSE is reduced by 40% and 31%, respectively. Similarly, it cuts the mean translation error by 45% versus *Constant* and 9% versus *Forward*, while the mean rotation error decreases by 35% and 27% compared with the same baselines.

Fig. 6a compares the estimated position trajectories and camera orientations produced by the two baselines and our planner for the “winter” reference trajectory. Fig. 6b plots the resulting translation and rotation errors over time. Our method tracks the path most accurately and achieves the lowest error, whereas *Constant* and

*Forward* attains lower accuracy compared to our method.

Consequently, the simulation results show that our perception-aware trajectory increases the localization accuracy.

**Computation time.** We break down the runtime of the three main modules in our pipeline. The average runtimes for (1) SCR & PnP-RANSAC, (2) the fixed-lag smoothing, and (3) the trajectory optimizations are 62.2ms, 0.8ms, and 28.3ms, respectively. Given the execution periods of the optimization and SCR modules, the overall latency is sufficiently low for real-time implementation.

TABLE III: Ablation study. Translation and rotation RMSE and mean error are given in  $\text{cm}^\circ$ , respectively.

Method	IMU+SCR		SCR	
	RMSE ↓	Mean ↓	Median ↓	Mean ↓
Vanilla	22.6/4.4	20.3/3.9	10.1/0.9	13.7/1.2
+ OW	24.0/3.8	21.5/3.1	10.2/0.8	14.1/1.2
+ OW + OR	21.5/2.7	19.2/2.4	9.8/1.1	13.4/1.2
+ OW + OR + SC	22.8/3.6	20.6/3.1	10.1/1.1	13.7/1.2

**Ablation study.** To assess the impact of uncertainty modeling, we progressively activated three components and reported the results in Table III. *Vanilla* uses the perception-aware planner with the weight in Eq. (10) set to 1.0 and applies no entropy filtering in either the optimization stage or SCR. *OW* recovers the entropy weighting in Eq. (10). *OR* additionally discards

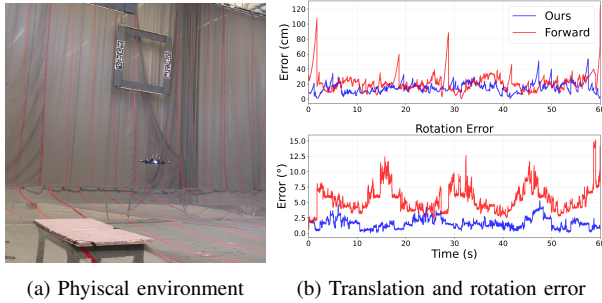


Fig. 7: Hardware-in-the-loop experiment. (a) Drone and spaces for the hardware-in-the-loop experiment. (b) Time histories of translation error (up) and rotation error (down) for Forward (red) and Ours (blue)

high-entropy pixels when sampling the  $n_f$  scene coordinates for the trajectory optimization; this is our full method. *SC* further excludes high-entropy points when sampling scene coordinates for PnP-RANSAC.

Enabling *OW* only reduces both rotation errors but increases the translation errors except the mean translation error of *SCR*. Introducing *OR* raises the median rotation errors of *SCR*, yet all other error metrics reach their lowest values, showing that the combination of entropy-based cost weights and discarding high-entropy samples during optimization yields the best localization accuracy. Adding *SC* causes a performance drop, suggesting that filtering high-entropy pixels may not be beneficial for PnP-RANSAC. Therefore, we demonstrate that utilizing entropy for the trajectory optimization increases the localization accuracy.

#### D. Hardware-in-the-loop Experiment

Fig. 7a illustrates our hardware-in-the-loop experiment setup. The quadrotor flies inside an arena while real IMU data are logged and the onboard camera streams images to the virtual *statal* scene. The vehicle follows a rose-petal trajectory,  $r = 3\cos(2\theta)$ , for three laps. Throughout the experiment, we compared the localization performance of the *Forward* baseline with that of our perception-aware trajectory planning framework.

In the experiment, our perception-aware trajectory planner performs better than the *Forward* baseline. Translation RMSE / mean error of the fused pose dropped from 26.3cm / 22.3cm to 20.7cm / 18.4cm, while rotational RMSE / mean error fell from 5.85° / 5.50° to 2.26° / 2.04°. Fig. 7b shows the errors over time for one lap of tracking the rose petal trajectory. The time histories in Fig. 7b show that the error of our approach remains consistently below that of the baseline throughout a representative lap, confirming the effectiveness and feasibility of the proposed method in a real flight.

## VI. CONCLUSION

This paper introduced a receding horizon, and perception-aware trajectory generation framework that contains evidential learning-based scene coordinate regression (SCR). The optimizer consistently oriented the camera toward scene coordinates with low uncertainty and produced drift-free, high-accuracy poses in real-time. Simulation and hardware-in-the-loop experiments demonstrate that our framework significantly outperforms baseline methods in localization accuracy and is suitable for real-world flight. Notably, these gains were achieved even though the SCR network was trained with only a small numbers of images, underscoring the framework’s suitability for data-scarce deployments. Future work will integrate obstacle avoidance, and test robustness to appearance changes such as lighting variations and object rearrangements.

## REFERENCES

- [1] Davide Falanga, Philipp Foehn, Peng Lu, and Davide Scaramuzza. Pampc: Perception-aware model predictive control for quadrotors. In *2018 IEEE/RSJ International Conference on Intelligent Robots and Systems (IROS)*, pages 1–8, 2018.
- [2] Zichao Zhang and Davide Scaramuzza. Perception-aware receding horizon navigation for mavs. In *2018 IEEE International Conference on Robotics and Automation (ICRA)*, pages 2534–2541, 2018.
- [3] Varun Murali, Igor Spasojevic, Winter Guerra, and Sertac Karaman. Perception-aware trajectory generation for aggressive quadrotor flight using differential flatness. In *2019 American Control Conference (ACC)*, pages 3936–3943, 2019.
- [4] Jamie Shotton, Ben Glocker, Christopher Zach, Shahram Izadi, Antonio Criminisi, and Andrew Fitzgibbon. Scene coordinate regression forests for camera relocalization in rgb-d images. In *Proceedings of the IEEE Conference on Computer Vision and Pattern Recognition (CVPR)*, June 2013.
- [5] Eric Brachmann, Alexander Krull, Sebastian Nowozin, Jamie Shotton, Frank Michel, Stefan Gumhold, and Carsten Rother. Dsac - differentiable ransac for camera localization. In *Proceedings of the IEEE Conference on Computer Vision and Pattern Recognition (CVPR)*, July 2017.
- [6] Eric Brachmann and Carsten Rother. Visual camera re-localization from rgb and rgb-d images using dsac. *IEEE Transactions on Pattern Analysis and Machine Intelligence*, 44(9):5847–5865, 2022.
- [7] Xiaotian Li, Shuzhe Wang, Yi Zhao, Jakob Verbeek, and Juho Kannala. Hierarchical scene coordinate classification and regression for visual localization. In *Proceedings of the IEEE/CVF Conference on Computer Vision and Pattern Recognition (CVPR)*, June 2020.
- [8] Shuzhe Wang, Zakaria Laskar, Iaroslav Melekhov, Xiaotian Li, Yi Zhao, Giorgos Tolias, and Juho Kannala. Hscnet++: Hierarchical scene coordinate classification and regression for visual localization with transformer, 2023.
- [9] Alexander Amini, Wilko Schwarting, Ava Soleimany, and Daniela Rus. Deep evidential regression. In H. Larochelle, M. Ranzato, R. Hadsell, M.F. Balcan, and H. Lin, editors, *Advances in Neural Information Processing Systems*, volume 33, pages 14927–14937. Curran Associates, Inc., 2020.
- [10] Luca Bartolomei, Lucas Teixeira, and Margarita Chli. Perception-aware path planning for uavs using semantic segmentation. In *2020 IEEE/RSJ International Conference on Intelligent Robots and Systems (IROS)*, pages 5808–5815, 2020.

- [11] Igor Spasojevic, Varun Murali, and Sertac Karaman. Perception-aware time optimal path parameterization for quadrotors. In *2020 IEEE International Conference on Robotics and Automation (ICRA)*, pages 3213–3219, 2020.
- [12] Zichao Zhang and Davide Scaramuzza. Fisher information field: an efficient and differentiable map for perception-aware planning, 2020.
- [13] Dabin Kim, Gyeong Chan Kim, Youngseok Jang, and H. Jin Kim. Topology-guided path planning for reliable visual navigation of mavs. In *2021 IEEE/RSJ International Conference on Intelligent Robots and Systems (IROS)*, pages 3117–3124, 2021.
- [14] Xinyi Chen, Yichen Zhang, Boyu Zhou, and Shaojie Shen. Apac: Agile and perception-aware trajectory generation for quadrotor flights. In *2024 IEEE International Conference on Robotics and Automation (ICRA)*, pages 17858–17864, 2024.
- [15] Chenxin Yu, Zihong Lu, Jie Mei, and Boyu Zhou. Perception-aware planning for quadrotor flight in unknown and feature-limited environments, 2025.
- [16] Dabin Kim, Inkyu Jang, Youngsoo Han, Sunwoo Hwang, and H. Jin Kim. Enhancing feature tracking reliability for visual navigation using real-time safety filter, 2025.
- [17] Alex Kendall, Matthew Grimes, and Roberto Cipolla. Posenet: A convolutional network for real-time 6-dof camera relocalization. In *Proceedings of the IEEE International Conference on Computer Vision (ICCV)*, December 2015.
- [18] Alex Kendall and Roberto Cipolla. Geometric loss functions for camera pose regression with deep learning. In *Proceedings of the IEEE Conference on Computer Vision and Pattern Recognition (CVPR)*, July 2017.
- [19] Florian Walch, Caner Hazirbas, Laura Leal-Taixe, Torsten Sattler, Sebastian Hilsenbeck, and Daniel Cremers. Image-based localization using lstms for structured feature correlation. In *Proceedings of the IEEE International Conference on Computer Vision (ICCV)*, Oct 2017.
- [20] Alex Kendall and Roberto Cipolla. Modelling uncertainty in deep learning for camera relocalization. In *2016 IEEE International Conference on Robotics and Automation (ICRA)*, pages 4762–4769, 2016.
- [21] Arthur Moreau, Nathan Piasco, Dzmitry Tsishkou, Bogdan Stanculescu, and Arnaud de La Fortelle. Coordinet: Uncertainty-aware pose regressor for reliable vehicle localization. In *Proceedings of the IEEE/CVF Winter Conference on Applications of Computer Vision (WACV)*, pages 2229–2238, January 2022.
- [22] Torsten Sattler, Qunjie Zhou, Marc Pollefeys, and Laura Leal-Taixe. Understanding the limitations of cnn-based absolute camera pose regression. In *Proceedings of the IEEE/CVF Conference on Computer Vision and Pattern Recognition (CVPR)*, June 2019.
- [23] Paul-Edouard Sarlin, Cesar Cadena, Roland Siegwart, and Marcin Dymczyk. From coarse to fine: Robust hierarchical localization at large scale. In *Proceedings of the IEEE/CVF Conference on Computer Vision and Pattern Recognition (CVPR)*, June 2019.
- [24] Yarin Gal and Zoubin Ghahramani. Dropout as a bayesian approximation: Representing model uncertainty in deep learning. In Maria Florina Balcan and Kilian Q. Weinberger, editors, *Proceedings of The 33rd International Conference on Machine Learning*, volume 48 of *Proceedings of Machine Learning Research*, pages 1050–1059, New York, New York, USA, 20–22 Jun 2016. PMLR.
- [25] Balaji Lakshminarayanan, Alexander Pritzel, and Charles Blundell. Simple and scalable predictive uncertainty estimation using deep ensembles. In I. Guyon, U. Von Luxburg, S. Bengio, H. Wallach, R. Fergus, S. Vishwanathan, and R. Garnett, editors, *Advances in Neural Information Processing Systems*, volume 30. Curran Associates, Inc., 2017.
- [26] Alex Kendall and Yarin Gal. What uncertainties do we need in bayesian deep learning for computer vision? In I. Guyon, U. Von Luxburg, S. Bengio, H. Wallach, R. Fergus, S. Vishwanathan, and R. Garnett, editors, *Advances in Neural Information Processing Systems*, volume 30. Curran Associates, Inc., 2017.
- [27] Juyeop Han, Lukas Lao Beyer, Guilherme V. Cavalheiro, and Sertac Karaman. Nvins: Robust visual inertial navigation fused with nerf-augmented camera pose regressor and uncertainty quantification. In *2024 IEEE/RSJ International Conference on Intelligent Robots and Systems (IROS)*, pages 12601–12608, 2024.
- [28] Bertrand Charpentier, Oliver Borchert, Daniel Zügner, Simon Geisler, and Stephan Günnemann. Natural posterior network: Deep bayesian uncertainty for exponential family distributions, 2022.
- [29] Le Chen, Weirong Chen, Rui Wang, and Marc Pollefeys. Leveraging neural radiance fields for uncertainty-aware visual localization. In *2024 IEEE International Conference on Robotics and Automation (ICRA)*, pages 6298–6305, 2024.
- [30] Siddharth Ancha, Philip R. Osteen, and Nicholas Roy. Deep evidential uncertainty estimation for semantic segmentation under out-of-distribution obstacles. In *2024 IEEE International Conference on Robotics and Automation (ICRA)*, pages 6943–6951, 2024.
- [31] Junyoung Kim, Junwon Seo, and Jihong Min. Evidential semantic mapping in off-road environments with uncertainty-aware bayesian kernel inference. In *2024 IEEE/RSJ International Conference on Intelligent Robots and Systems (IROS)*, pages 1420–1427, 2024.
- [32] Xiaoyi Cai, Siddharth Ancha, Lakshay Sharma, Philip R. Osteen, Bernadette Bucher, Stephen Phillips, Jiuguang Wang, Michael Everett, Nicholas Roy, and Jonathan P. How. Evora: Deep evidential traversability learning for risk-aware off-road autonomy. *IEEE Transactions on Robotics*, 40:3756–3777, 2024.
- [33] Daniel Mellinger and Vijay Kumar. Minimum snap trajectory generation and control for quadrotors. In *2011 IEEE International Conference on Robotics and Automation*, pages 2520–2525, 2011.
- [34] Frank Dellaert and GTSAM Contributors. borglab/gtsam, May 2022.
- [35] Ezra Tal and Sertac Karaman. Accurate tracking of aggressive quadrotor trajectories using incremental nonlinear dynamic inversion and differential flatness. *IEEE Transactions on Control Systems Technology*, 29(3):1203–1218, 2021.
- [36] Winter Guerra, Ezra Tal, Varun Murali, Gilhyun Ryou, and Sertac Karaman. Flightgoggles: Photorealistic sensor simulation for perception-driven robotics using photogrammetry and virtual reality. In *2019 IEEE/RSJ International Conference on Intelligent Robots and Systems (IROS)*, pages 6941–6948, 2019.
- [37] Amado Antonini, Winter Guerra, Varun Murali, Thomas Sayre-McCord, and Sertac Karaman. The blackbird uav dataset. *The International Journal of Robotics Research*, 39(10-11):1346–1364, 2020.
- [38] Steven G. Johnson. The NLOpt nonlinear-optimization package, 2007.